Mean-field approximation of network of biophysical neurons driven by conductance-based ion exchange

Abhirup Bandyopadhyay [*], Giovanni Rabuffo [*], Carmela Calabrese , Kashyap Gudibanda , Damien Depannemaecker , Anton Ivanov , Christophe Bernard , Viktor K. Jirsa [+], and Spase Petkoski [+]

Aix Marseille University, INSERM, Institute de Neuroscience des Systems, Marseille, 13005 France
[*]These authors contributed equally to this work as first author
[+]These authors contributed equally to this work as last author
[+]e-mail: viktor.jirsa@univ-amu.fr , spase.petkoski@univ-amu.fr

ABSTRACT

Numerous network and whole-brain modeling approaches use mean-field models, facilitating the study of dynamics due to their relative simplicity. They correspond to lumped descriptions of neuronal assemblies connected via synapses. Mean-field models do not usually consider the ionic composition of the extracellular space, which can change in physiological and pathological conditions, with strong effects on neuronal activity. Here we derive a mean-field model of a population of Hodgkin–Huxley type neurons, which links the neuronal intra- and extra-cellular ion concentrations to the mean membrane potential and the mean synaptic input in terms of the synaptic conductance. Thus, the model provides a mean-field approximation, for locally homogeneous mesoscopic networks of biophysical neurons driven by an ion-exchange mechanism. The model can generate various physiological brain activities, including multi-stability during simulated healthy states, pathological spiking, bursting behaviors, and depolarization block. The results from the analytical solution of the mean-field model agree with the mean behavior of numerical simulations of large-scale networks of strongly synchronized neurons. The mean-field model exhibits emergent activity regimes qualitatively similar to those observed in weakly synchronized neuronal networks and experimentally observed *in-vitro*. This approach maintains a detailed biophysical level of description, such as the evolution of ionic concentrations while describing dynamics at the neural mass scale. Hence, these results may provide the missing link between high-level neural mass approaches, used in brain network modeling, and physiological parameters that drive the neuronal dynamics.

Key words: Hodgkin–Huxley-type neurons, Mean-field model, Biophysical neural mass modeling, Multiscale neural mechanisms, Epilepsy

Significance Statement: In this study, we applied a mathematical formalism to estimate the mean-field behavior of a large neuronal ensemble, taking into account the ion exchange between the intracellular and extracellular space. This approach establishes a link between the biophysical description at the cellular scale and the dynamics observable at the mesoscopic scale. The model reproduces different brain activities, including spiking behavior, and seizures, as a function of the extracellular ion concentration. Thus, this neural mass model enables studying the influence of changes in extracellular ionic conditions on whole brain dynamics in health and disease.

Introduction

Large-scale brain dynamics can be studied in silico with network models (Deco et al., 2011). Local activity can be represented by neuronal mass models (Deco et al., 2008), which coupled together through synapses, time delays and noise (Deco and Jirsa, 2012, Petkoski and Jirsa, 2019) allow the emergence of whole brain activity that can be linked to empirical neuroimaging data (Sanz-Leon et al., 2015). The observable properties (variables) in the population level of a large-scale ensemble are generally explained by statistical physics formalism of mean-field theory (Wilson and Cowan, 1972, David and Friston, 2003, Moran et al., 2007, Wong and Wang, 2006). These models demonstrated a predictive value for resting-state brain activity (i.e., in the absence of any stimulus or task) (Melozzi et al., 2019, Courtiol et al., 2020, Rabuffo et al., 2021), or for seizure genesis and propagation in epilepsy, (Proix et al., 2017). Neural mass models have a low enough number of parameters to be tractable and

provide general intuitions regarding mechanisms underlying complex brain activity (Jirsa et al., 2014, Jirsa et al., 2017, Deco et al., 2021, Amunts et al., 2020, Depannemaecker et al., 2021a, Carlu et al., 2020). Although it is practically inconvenient to reproduce the entire complexity of the brain including all known biophysical parameters, it may be important to include parameters that can have widespread and general effects on neuronal activity (Amunts et al., 2020).

The concentration of Na^+, K^+, Ca^{2+}, and Cl^- ions in the extracellular space is one of the key parameters to consider. Extracellular ion concentrations change dynamically in vivo as a function of the brain state, for example between arousal and sleep (Ding et al., 2016, Rasmussen et al., 2017). Changes in extracellular ion concentrations can induce fluctuations in awake state (Rasmussen et al., 2019, Krishnan et al., 2018) as well as switch one brain state to another (Ding et al., 2016). In particular, the extracellular potassium concentration $[K^+]_{ext}$ plays a central role. Transient changes in $[K^+]_{ext}$ can have large effects on cell excitability and spontaneous neuronal activity (Amzica et al., 2002, Ransom et al., 2000, Cressman et al., 2009), a result consistently reported in modeling studies (Bazhenov et al., 2004, Park and Durand, 2006, Fröhlich et al., 2008). Increases in $[K^+]_{ext}$ are tightly controlled by astrocytes (Orkand et al., 1966), which can efficiently pump $[K^+]_{ext}$ and distribute it via their syncytium to prevent hyperexcitability (Breslin et al., 2018, Nwaobi et al., 2016, Crunelli et al., 2015, Hansson et al., 2000, Bedner and Steinhäuser, 2013). The saturation or lack of efficiency of these buffering mechanisms is often linked to a pathological state. Detailed single neuron models demonstrate that continuous increases in $[K^+]_{ext}$ can lead to different firing states, from tonic to bursting, to seizure-like events and depolarization block (Cressman et al., 2009, Depannemaecker et al., 2021b). In such detailed models, the buffering action of astrocytes is represented by a parameter named $[K^+]_{bath}$ (Cressman et al., 2009, Breslin et al., 2018, Ullah et al., 2009, Nwaobi et al., 2016, Depannemaecker et al., 2021b). This parameter may also account for the potassium concentration in the perfusion bath in *in vitro* studies Our goal is to use a similar approach but at the neural mass model level, to be incorporated to study whole-brain dynamics.

Phenomenological neuron models have been studied to understand the macroscopic dynamics of neuronal populations (Izhikevich and Edelman, 2008) or to provide statistical descriptions of neuronal networks (Wilson and Cowan, 1972, Deco et al., 2008, Montbrió et al., 2015, Montbrió and Pazó, 2020). Statistical population measures, such as the firing rate, can be used to assess macroscopic dynamics (Shriki et al., 2003, Deco et al., 2011, Roxin et al., 2005, Luke et al., 2013, Jirsa et al., 2014, Proix et al., 2014, Sanz-Leon et al., 2015, Wendling et al., 2016, Ashwin et al., 2016, Carlu et al., 2020). Recent studies combine local neuronal dynamics with statistical descriptions in terms of the mean membrane potential and the firing rate in quadratic integrate-and-fire (QIF) neurons (Montbrió et al., 2015, Devalle et al., 2018, Montbrió and Pazó, 2020). Neural mass models are also used in the context of large-scale brain simulations for the analysis and identification of chaos in brain signals (Baladron et al., 2012, Bandyopadhyay and Kar, 2018), epileptic seizure transmission (Spiegler et al., 2011, Touboul et al., 2011, Nevado-Holgado et al., 2012, Hocepied et al., 2013, El Houssaini et al., 2015a), phase oscillations (Laing, 2017, Byrne et al., 2017, Petkoski and Stefanovska, 2012), the evolution of network synchrony (Bandyopadhyay and Kar, 2018, Petkoski and Stefanovska, 2012) and several other problems. Here we approximate the membrane potential dynamics of Hodgkin-Huxley neurons by a step-wise quadratic model equipped with two slow biophysical variables modeling ion-exchange dynamics. The distribution of the neurons' membrane potentials is described by a Lorentzian ansatz (LA), which allows the analytical solution of the continuity equation, leading to mean-field equations for the population. The model provides a mean-field approximation within the thermodynamic limit, i.e., for a locally homogeneous mesoscopic neuronal network (Fig 1). We demonstrate that our model captures the behavior of an all-to-all coupled network of heterogeneous Hodgkin-Huxley neurons thus describing the ion-exchange-driven neuronal dynamics. Considering different parameter configurations, we characterize the macroscopic states of the recurrently connected neurons, in various dynamical regimes that can be linked to different healthy and pathological states and be of use in large-scale brain simulations.

Materials and Methods

Immature hippocampus in vitro preparation

All protocols were designed and approved according to INSERM and international guidelines for experimental animal care and use. Experiments were performed on intact hippocampi taken from FVB NG mice between postnatal (P) days 5 and 7 (P0 was the day of birth). The immature mice were decapitated rapidly, and the brain was extracted from the skull and transferred to oxygenated (95% O_2 / 5% CO_2) ice cold (4 °C) artificial cerebrospinal fluid (aCSF) containing (in mM): NaCl 126; KCl 3.5; $CaCl_2$ 2.0; $MgCl_2$ 1.3; $NaHCO_3$ 25; $NaHPO_4$ 1.2; glucose 10 (pH = 7.3). After at least 2 hours of incubation at room temperature in aCSF, hippocampi were transferred to the recording chamber. To ensure a high perfusion rate (15 ml/min) we used a closed-circuit perfusion system with recycling driven by a peristaltic pump: 250 ml of solution was used per hippocampus and per condition. The pH (7.3) and temperature (33 °C) were controlled during all experiments.

Induction of epileptiform events

After 30 min baseline recording in Mg^{2+} containing aCSF solution, the media was switched to one without adding Mg^{2+} ion. In this condition, the extracellular concentration of Mg^{2+} may be influenced by other constituents of the aCSF, possibly near 0.08

mM (Mody et al., 1987). Therefore, we use the term low- Mg^{2+} aCSF rather than zero-Mg^{2+} aCSF.

Electrical activity monitoring

Extracellular glass electrode filled with low Mg^{2+} aCSF was placed into the mid CA1 region of the ventral hippocampus. Local field potentials (LFPs) were amplified with a MultiClamp700B (Molecular Devices, San Jose, CA) amplifier for DC-coupled recording, then digitized with a Digidata 1440 (Molecular Devices, San Jose, CA), stored on the hard drive of the personal computer and displayed using PClamp 9 software (Molecular Devices, San Jose, CA).

External Potassium concentration Measurements

Potassium-selective microelectrodes were prepared using the method described by Heinemann and Arens. In brief, electrodes were pulled from double-barrel theta glass (TG150-4, Warner Instruments, Hamden, CT, USA). The reference barrel was filled with 154 mM NaCl solution. The silanized ion-sensitive barrel tip (5% trimethyl-1-chlorosilane in dichloromethane)was filled with a potassium ionophore I cocktail A (60031 Fluka distributed by Sigma-Aldrich, Lyon, France) and backfilled with 100 mM KCl. Measurements of $[K^+]_{ext}$-dependent potentials were performed using a high-impedance differential DC amplifier (kindly provided by Dr. U Heinemann (Heinemann and Arens, 1992)) equipped with negative capacitance feedback control, which permitted recordings of relatively rapid changes in $[K^+]_{ext}$ (time constants 50–200 ms). The electrodes were calibrated before each experiment and had a sensitivity of 42-63 mV/mM. The tip of the electrode was placed into the CA1 region of the ventral hippocampus at 200-300µm distance from the LFP recording electrode at 150-200 µm depth that, at P5-P6 age, corresponds to the Stratum Radiatum.

Biophysical neuron model

The membrane potential of a single neuron in the brain is related to an ion-exchange mechanism in intracellular and extracellular space. The concentrations of potassium, sodium, and chloride in the intracellular and extracellular space along with the active transport pump (Na^+/K^+ pump) in the cell membrane of neurons generate input currents that drive the electrical behavior in terms of the evolution of its membrane potential. The ion-exchange mechanisms in the cellular microenvironment, including local diffusion, glial buffering, ion pumps, and ion channels, have been mathematically modeled based on conductance-based ion dynamics to reflect the 'healthy' and seizure behaviors in single neurons (Hodgkin and Huxley, 1952, Cressman et al., 2009, Ullah et al., 2009, Depannemaecker et al., 2021b). The mechanisms of ion exchange in the intracellular and extracellular space of the neuronal membrane are represented schematically in Fig. 1. This biophysical interaction and ion-exchange mechanism across the membrane of a neuronal cell can be described as a Hodgkin–Huxley type dynamical process, represented by the following dynamical system (1; (Depannemaecker et al., 2021b)).

$$\begin{aligned}
\frac{\mathrm{d}V}{\mathrm{d}t} &= -\frac{1}{C_m}(I_{Cl}+I_{Na}+I_K+I_{pump}) \\
\frac{\mathrm{d}n}{\mathrm{d}t} &= \frac{n_\infty(V)-n}{\tau_n} \\
\frac{\mathrm{d}\Delta[K^+]_{int}}{\mathrm{d}t} &= -\frac{\gamma}{\omega_i}(I_K-2I_{pump}) \\
\frac{\mathrm{d}[K^+]_g}{\mathrm{d}t} &= \varepsilon([K^+]_{bath}-[K^+]_{ext})
\end{aligned} \tag{1}$$

This model represents the ion-exchange mechanism of a single conductance-based neuron in terms of membrane potential V, the potassium conductance gating variable n, intracellular potassium concentration variation $\Delta[K^+]_{int}$ and extracellular potassium buffering by the external bath $[K^+]_g$. This mechanism considers ion exchange through the chloride, sodium, potassium, voltage-gated channels, intracellular sodium, and extracellular potassium concentration gradients and leak currents. The intrinsic ionic currents of the neuron along with the sodium-potassium pump current and potassium diffusion regulate the different ion concentrations. The Nernst equation was used to couple the membrane potential of the neuron with the concentrations of the ionic currents. This mechanism gives rise to a slow-fast dynamical system in which the membrane potential V and potassium conductance gating variable n constitute the fast subsystem and the slow subsystem is represented in terms of the variation in the intracellular potassium concentration $\Delta[K^+]_{int}$ and extracellular potassium buffering by the external bath $[K^+]_g$ (Fig. 2.b). In Eq. (1) the input currents due to different ionic substances and pump are represented as

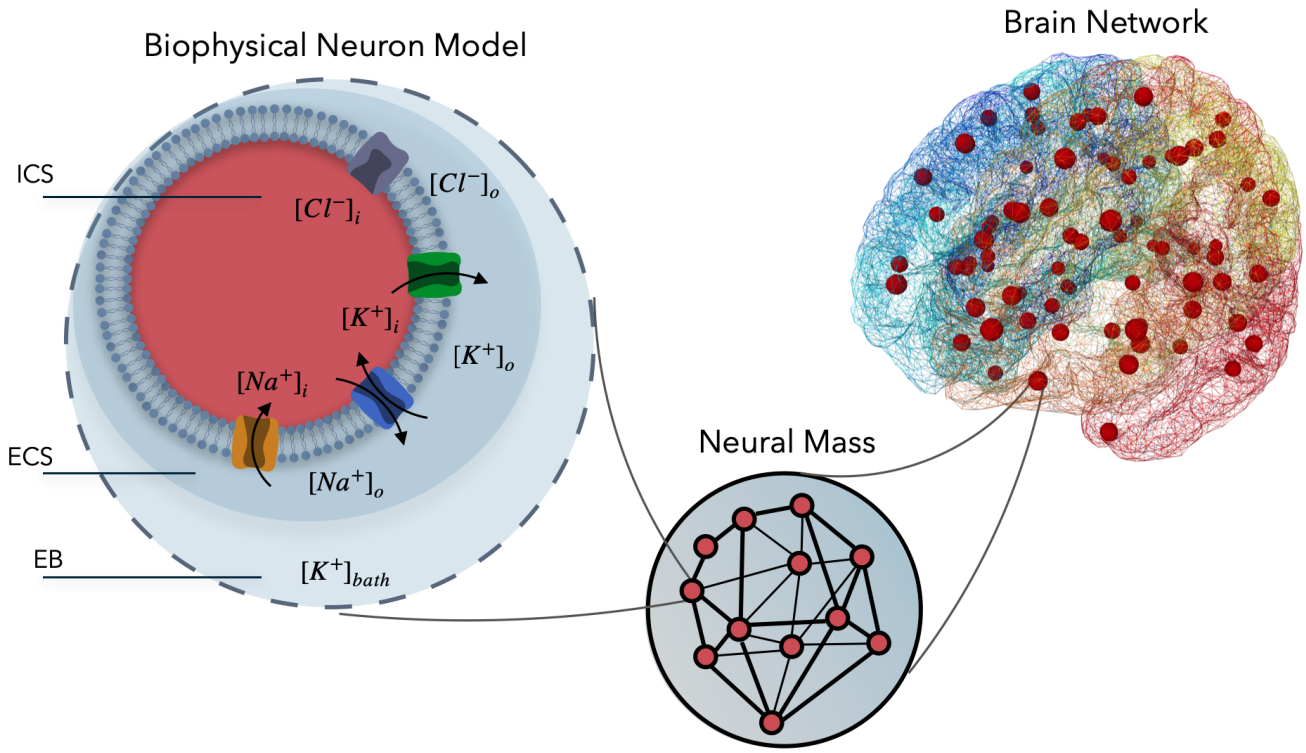

Figure 1. Biophysically inspired neural mass model: Schematic diagram of the ion channel mechanism in extracellular and intracellular space in the brain. A biophysical model of a single neuron consists of three compartments (left panel): the intracellular space (ICS; in red), the extracellular space (ECS; in dark blue), and the external bath (EB; in light blue). The ion exchange across the cellular space occurs through the ion channels: Na^+ gets inside the ICS (yellow channel), K^+ gets out (green channel), the flow of Cl^- can be bidirectional (purple channel); for the pump (blue), Na^+ gets out and K^+ gets into the ICS. A population of interacting neurons sharing the same $[K^+]_{bath}$ concentration forms a local neural mass (middle panel), for which we model the mean-field equations in this work. Brain network model (right panel) with the activity of each brain region represented by neural masses.

follows (Cressman et al., 2009, Depannemaecker et al., 2021b):

$$\begin{aligned}
I_{Na} &= (g_{Na,l} + g_{Na} m_\infty(V) h(n))\Big(V - 26.64 \log\Big(\frac{[Na^+]_{ext}}{[Na^+]_{int}}\Big)\Big),\\
I_K &= (g_{K,l} + g_K n)\Big(V - 26.64 \log\Big(\frac{[K^+]_{ext}}{[K^+]_{int}}\Big)\Big),\\
I_{Cl} &= g_{Cl}\Big(V + 26.64 \log\Big(\frac{[Cl^-]_{ext}}{[Cl^-]_{int}}\Big)\Big),\\
I_{pump} &= \rho \frac{1}{1+\exp(10.5 - 0.5[Na^+]_{int})} \frac{1}{1+\exp(5.5 - [K^+]_{ext})}.
\end{aligned} \tag{2}$$

The gating functions for the conductance are modeled as:

$$\begin{aligned}
n_\infty(V) &= \frac{1}{1+\exp(\frac{-30-V}{5})},\\
m_\infty(V) &= \frac{1}{1+\exp(\frac{-22-V}{15})},\\
h(n) &= 1.1 - \frac{1}{1+\exp(-8(n-0.4))}.
\end{aligned} \tag{3}$$

In this model the concentration of chloride ions inside and outside of the membrane is invariant. i.e., $[Cl^-]_{ext} = [Cl^-]_{0,ext}$ and

$[Cl^-]_{int} = [Cl^-]_{0,int}$. The extracellular and intracellular concentrations of sodium and potassium ions are represented in terms of the state variables $\left(\Delta[K^+]_{int}, [K^+]_g\right)$ as follows:

$$\begin{aligned}
\Delta[Na^+]_{int} &= -\Delta[K^+]_{int} \\
\Delta[Na^+]_{ext} &= -\beta\,\Delta[Na^+]_{int} \\
\Delta[K^+]_{ext} &= -\beta\,\Delta[K^+]_{int} \\
[K^+]_{int} &= K_{i0} + \Delta[K^+]_{int} \\
[Na]_{int} &= Na_{i0} + \Delta[Na^+]_{int} \\
[Na^+]_{ext} &= [Na^+]_{0,ext} + \Delta[Na^+]_{ext} \\
[K^+]_{ext} &= [K^+]_{0,ext} + \Delta[K^+]_{ext} + [K^+]_g
\end{aligned} \tag{4}$$

The biophysically relevant values of the parameters could be obtained from several previous studies, both from in vivo and in vitro experiments (Cressman et al., 2009). The parameters used for the single-neuron simulations are shown in Table-1, and allow the reproduction of several bursting and oscillatory regimes by varying the parameter $[K^+]_{bath}$ (Fig. 2.a).

Parameter	Symbol	Value
Membrane capacitance	C_m	$1n$F
Gating time constant	τ_n	$4m$s
Chloride conductance	g_{Cl}	$7.5n$S
Maximal potassium conductance	g_K	$22n$S
Maximal sodium conductance	g_{Na}	$40n$S
Potassium leak conductance	$g_{K,l}$	$0.12n$S
Sodium leak conductance	$g_{Na,l}$	$0.02\ n$S
Intracellular volume	ω_i	2160μm^3
Extracellular volume	ω_{ext}	720μm^3
Intra/extra-cellular volume ratio	$\beta = \omega_i/\omega_{ext}$	3
Conversion factor	γ	0.04 mol/C
Diffusion rate	ε	$0.001m$Hz
Maximal Na/K pump current	ρ	$250p$A
Initial concentration of Extracellular K	$[K^+]_{0,ext}$	4.8 $m$mol/m^3
Initial concentration of Intracellular K	$[K^+]_{0,int}$	130 $m$mol/m^3
Initial concentration of Extracellular Na	$[Na^+]_{0,ext}$	138 $m$mol/m^3
Initial concentration of Intracellular Na	$[Na^+]_{0,int}$	16 $m$mol/m^3
Initial concentration of Extracellular Cl	$[Cl^-]_{0,ext}$	112 $m$mol/m^3
Initial concentration of Intracellular Cl	$[Cl^-]_{0,int}$	5 $m$mol/m^3

Table 1. List of parameters and their values used for the single-neuron simulation.

Network of coupled biophysical neurons

Our aim is to develop a mean-field model for a heterogeneous population of the all-to-all coupled biophysical neurons described by Eq. (1). Our strategy consists of using a series of approximations to obtain a putative functional form for the mean-field model, which is capable of simulating the mean activity of a large population of HH neurons. As a first step, we need to model the synaptic kinetics in terms of the model variables. The basic mechanism of synaptic transmission can be described by the arrival of a spike at the presynaptic terminal, resulting in an influx of calcium which depolarizes the presynaptic terminals and thus stimulates the release of neurotransmitters into the synaptic cleft. The neurotransmitters play a crucial role in opening the postsynaptic channels, which causes the flow of ionic currents across the membrane. This flow creates an (inhibitory or excitatory) post-synaptic potential in the efferent neuron. We take this into account by adding a synaptic input current in the membrane potential equation. It can be modeled at neuron i thanks to a conductance-based model as

$$I_{syn} = g_{syn,i}(t)(E_{syn} - V_i), \tag{5}$$

where $g_{syn,i}$ is the synaptic conductance, V_i is the postsynaptic potential and E_{syn} is the synaptic reversal potential at which the direction of the net current flow reverses. Typically, at the arrival time t_j^k of the k-th spike from neuron j, the synaptic

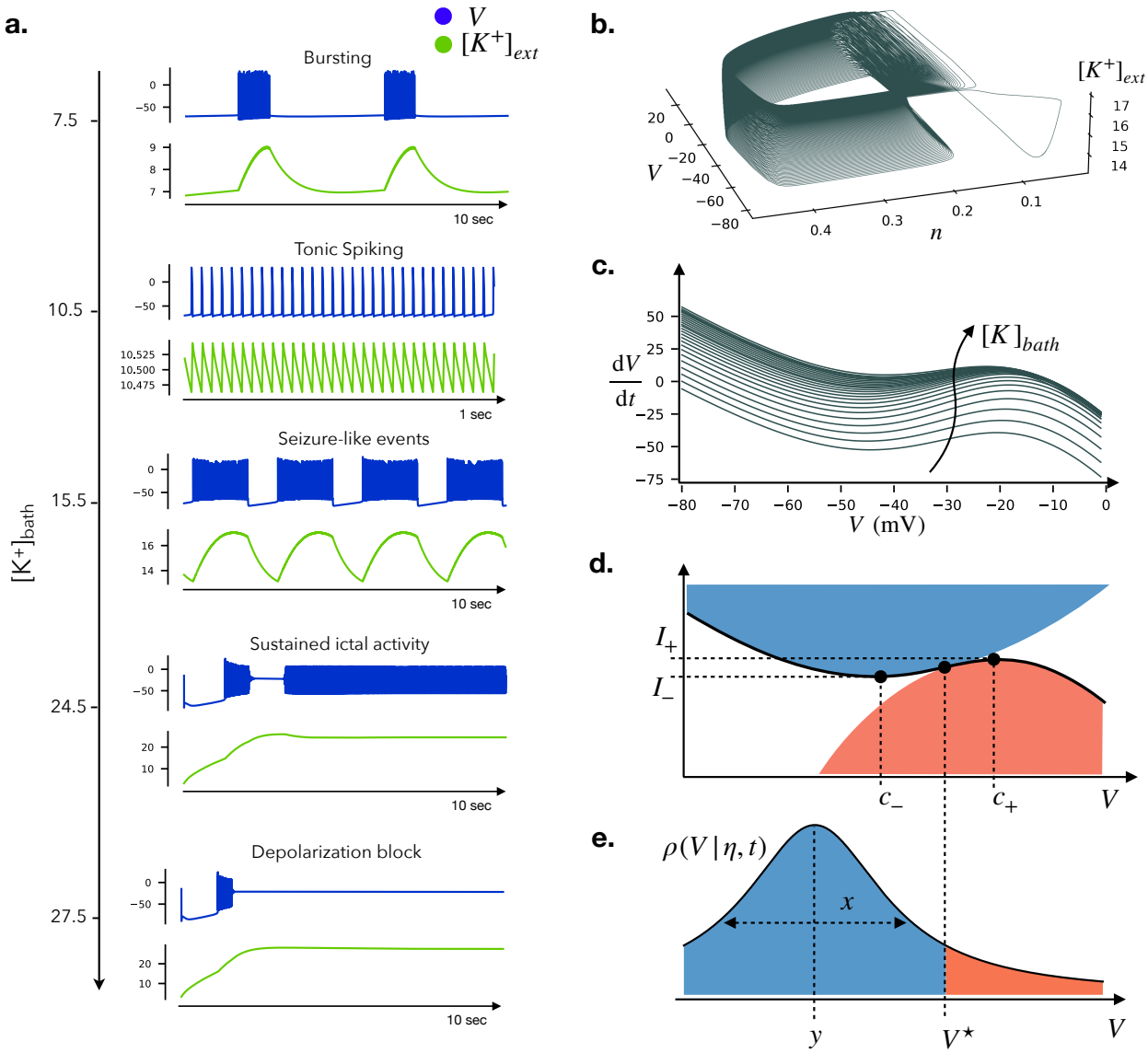

Figure 2. Single Hodgkin-Huxley-like neuron model: (a) Different patterns of electrophysiological activities previously identified (Depannemaecker et al., 2021b) are also reproduced in our parameter setting. Voltages are measured in mV and ion concentrations in $m$mol/m^3.(b) Phase space trajectory of the seizure-like event simulation ($[K^+]_{bath} = 15.5$). Fast oscillations occur in a fast sub-system (V and n), whereas the oscillations of the slow subsystem (here captured by $[K^+]_{ext}$) enable the transition to bursting. (c) Fixing $n, \Delta[K^+]_{int}$ and $[K^+]_g$ as constants, the membrane potential equation resembles a cubic function for different values of $[K^+]_{bath}$. We can model this function as a step-wise quadratic approximation, corresponding to two parabolas with vertices at coordinates (c_-, I_-) and (c_+, I_+) and curvature R_- and R_+ respectively (d). The two parabolas meet at an intersection point $V^\star$ where the membrane potential equation changes curvature. (e) In the Lorentzian Ansatz (LA) the membrane potential of a neuronal population is distributed according to a Lorentzian centered at $y = y(\eta, t)$ and with width $x = x(\eta, t)$, for each value of the noise η.

conductance quickly rises and consequently undergoes an exponential decay with some rate constant. This mechanism is captured by defining the conductance dynamics $g_{syn,i} \propto s_i(t)$ where the adimensional dynamical variable $s_i(t)$ is the solution of the following equation:

$$Qs_i(t) = J\sum_{j=1}^{N}\sum_{k} W_{ij}\delta(t-t_j^k), \tag{6}$$

where J is the synaptic strength, W_{ij} is the synaptic weight which here we assume to be equal to 1 for all neurons i and j, and the operator Q can be defined with various levels of accuracy as

$$Q=1, \quad Q=\left(1+\tau_s\frac{\mathrm{d}}{\mathrm{d}t}\right), \quad Q=\left(1+\tau_{s_1}\frac{\mathrm{d}}{\mathrm{d}t}\right)\left(1+\tau_{s_2}\frac{\mathrm{d}}{\mathrm{d}t}\right), \quad \dots \tag{7}$$

Here, for simplicity, we select the first model, which leads to

$$s_i = J\sum_{j=1}^{N}\sum_{k}\delta(t-t_j^k). \tag{8}$$

In the coupled system, the membrane potential equation for neuron i is defined by:

$$\frac{dV_i}{dt} = -\frac{1}{C_m}\left(I_{Cl,i}+I_{Na,i}+I_{K,i}+I_{pump,i}\right)+Js_i(E_{syn}-V_i)+\eta_i \tag{9}$$

where the constant ν has the dimension of a frequency, and the term η_j represents an heterogeneous excitability distributed according to a Lorentzian distribution

$$g(\eta) = \frac{1}{\pi}\frac{\Delta}{(\eta-\bar{\eta})^2+\Delta^2}, \tag{10}$$

with half-width Δ and location of the center at $\bar{\eta}$.

Continuous formulation

In the limit of large population $N\to\infty$, the variables will become continuous and we can drop the i-indices. In order to perform the thermodynamic limit we assume that the distribution of membrane potentials for neurons receiving a heterogeneous input η is independent of the gating variable and potassium dynamics:

$$\rho(V|n,\Delta[K^+]_{int},[K^+]_g,\eta,t) \simeq \rho(V|\eta,t), \tag{11}$$

and satisfies the continuity equation:

$$\partial_t\rho + \partial_V(\rho\dot{V}) = 0. \tag{12}$$

This equation can be solved if the distribution is a Lorentzian and if the $\dot{V}$ equation is a quadratic function of the membrane potential V (Montbrió et al., 2015). However, the typical form of equation (9)–for constant gating and potassium variables–resembles a cubic function of V (Fig. 2.c; see also Suppl.Fig S1). Our strategy is to approximate equation (9) by a step-wise quadratic function, corresponding to two parabolas with opposite curvature intersecting at $V=V^\star$ (Fig. 2.d; see next section). Then, on either side of the threshold $V^\star$ we impose a Lorentzian Ansatz i.e., we assume that the distribution of membrane potential for neurons with excitability η is of the form:

$$\rho(V|\eta,t) = \frac{1}{\pi}\frac{x(\eta,t)}{(V-y(\eta,t))^2+x(\eta,t)^2}, \tag{13}$$

where $x(\eta,t)$ and $y(\eta,t)$ represent the width and the mean of the distribution, respectively (Fig. 2.e). With these assumptions, we will derive the mean-field model equations in the next sections.

Stepwise quadratic approximation

In order to solve the continuity equation (12) we want to write the equation (9) as an explicit function of V, which has to be quadratic. For a decoupled system described by Eqs. (1), considering the gating variables and the potassium variables as generic constants (i.e., studying the nullcline geometry), the equation for the membrane potential $\dot{V}_0$ has the profile of a cubic function.

In Fig. 2.c we show examples of cubic functions associated with distinct values of the parameter $[K^+]_{bath}$, where the variables $\left(\Delta[K^+]_{int}, [K^+]_g\right)$ were fixed to constant values corresponding to the time average of their simulated decoupled activity (as in Fig. 2.a), while the gating variable n was fixed to its maximum value. We can fit the nullcline geometry for the uncoupled neuron dynamics (without I_{syn}) as:

$$\frac{\mathrm{d}V_0}{dt} = \begin{cases} R_-(V-c_-)^2 + I_- \,; & \forall V_0 \leq V^\star \\ R_+(V-c_+)^2 + I_+ \,; & \forall V_0 > V^\star \end{cases} \tag{14}$$

corresponding to two parabolas with opposite curvature ($R_- > 0, R_+ < 0$), centered at c_- and c_+ and shifted by I_+ and I_-, respectively (Fig. 2.d). In general, the coefficients of the parabolas $(c_\pm, I_\pm, R_\pm)$ would be functions of the fast gating variable n and of the slow potassium variables $\left(\Delta[K^+]_{int}, [K^+]_g\right)$ (see also Suppl. Fig. S1.b-c). In our approximation in Fig. 2.d they are coefficients that only depend on the parameter $[K^+]_{bath}$. For each $[K^+]_{bath}$, we numerically estimated the (c_-, I_-) and (c_+, I_+) coordinates (Suppl. Fig. S1.a). The intersection point of the two parabolas, called $V^\star$, was estimated as the point where the $\dot{V}_0$ function changes curvature i.e.,

$$\left.\frac{\partial^2 \dot{V}_0}{\partial V}\right|_{V^\star} = 0. \tag{15}$$

The two curvatures were derived by imposing that the two parabolas have the same derivative in $V^\star$ i.e.,

$$\left.\partial_V \dot{V}_0\right|_{V^{\star -}} = \left.\partial_V \dot{V}_0\right|_{V^{\star +}} \implies R_-(V^\star - c_-) = R_+(V^\star - c_+) \implies V^\star = \frac{R_- c_- - R_+ c_+}{R_- - R_+}, \tag{16}$$

and that they touch on this point i.e.,

$$\left.\dot{V}_0\right|_{V^{\star -}} = \left.\dot{V}_0\right|_{V^{\star +}} \implies R_-(V^\star - c_-)^2 + I_- = R_+(V^\star - c_+)^2 + I_+ \implies \frac{I_+ - I_-}{(c_+ - c_-)^2} = \frac{R_+^2 R_- - R_+ R_-^2}{(R_+ - R_-)^2}. \tag{17}$$

This way, we obtained the following conditions for the curvature:

$$R_+ = R_- \frac{(V^\star - c_-)}{(V^\star - c_+)} = \frac{I_+ - I_-}{(c_+ - c_-)(V^\star - c_+)}. \tag{18}$$

Here, for simplicity, we fixed the values of the estimated $(c_\pm, I_\pm, R_\pm)$ coefficients by averaging over values of $[K^+]_{bath} \in [3.5, 27.5]$, thus obtaining an approximate configuration

$$\begin{cases} c_- = -44.24, & I_- = -213.1, & R_- = 0.337, \\ c_+ = -20.40, & I_+ = -106.6, & R_+ = -0.381. \end{cases} \tag{19}$$

These values will appear in the mean-field model and can be tuned to fit the average activity of a large neuronal network.

Mean-field variables and firing rate

Next, we consider a system of coupled neurons interacting via their synaptic input currents (5) and affected by Lorentzian noise (10). For a given value of η the neurons' firing rate is given by the probability flux at the threshold V_{th}:

$$r(\eta, t) = \rho(V \to V_{th} | \eta, t) \dot{V}(V \to V_{th}), \tag{20}$$

Here, we define the firing rate based on the positive parabolic trend of $\dot{V}$ i.e., for $V < V^\star$, and setting the threshold at $V_{th} \to \infty$ as typically assumed in the thermodynamic limit of QIF populations (as in (Montbrió et al., 2015)). Therefore, we obtain the following definition of firing rate:

$$r(\eta, t) = \frac{R_- x(\eta, t)}{\pi} \tag{21}$$

In the thermodynamic limit, the mean-field variables correspond to:

$$\begin{aligned} x(t) &= \int x(\eta, t) g(\eta) \mathrm{d}\eta, \\ y(t) &= \int y(\eta, t) g(\eta) \mathrm{d}\eta, \\ r(t) &= \int r(\eta, t) g(\eta) \mathrm{d}\eta. \end{aligned} \tag{22}$$

The integrals (22) can be evaluated by using the residue theorem. Since there is only one pole of $g(\eta)$ in the complex η-plane, we obtain that integrating out η corresponds to substituting $\eta = \overline{\eta} - i\Delta$. Therefore,

$$\begin{aligned} x(t) &= x(\bar{\eta} - i\Delta, t), \\ y(t) &= y(\bar{\eta} - i\Delta, t), \\ r(t) &= \frac{R_- x(t)}{\pi}. \end{aligned} \tag{23}$$

Derivation of mean-field equations

Starting from equations (14) and (5) the membrane potential dynamics for a coupled system of neurons is described on either side of the intersection point $V^\star$ by the following equation:

$$\frac{\mathrm{d}V}{dt} = AV^2 + BV + C \tag{24}$$

with

$$\begin{aligned} A &= R, \\ B &= -2Rc - Jr, \\ C &= Rc^2 + I + JrE + \eta. \end{aligned} \tag{25}$$

The parameters (R, c, I) were introduced in the previous section as the curvature, center, and shift of the parabolas in the step-wise approximation. Here the indices $(-,+)$ were dropped for simplicity.

Substituting equations (24) and (13) in the continuity equation (12) we obtain a polynomial condition of the form

$$k_3 V^3 + k_2 V^2 + k_1 V + k_0 = 0. \tag{26}$$

The mean-field equations for $x(\eta, t)$ and $y(\eta, t)$ are obtained by imposing $k_I \equiv 0, \forall I = 0, 1, 2, 3$, leading to

$$\begin{aligned} \dot{x} &= 2Axy + Bx, \\ \dot{y} &= Ay^2 + By + C - Ax^2. \end{aligned} \tag{27}$$

Defining $\omega(\eta, t) = x(\eta, t) + iy(\eta, t)$, we can recast the above equations in the complex form

$$\dot{\omega} = i\big(C - A\omega^2 - iB\omega\big). \tag{28}$$

The mean-field equations are derived by integrating out η from the equation above. According to (23), we find $\omega(\overline{\eta} - i\Delta, t) = x(t) + iy(t)$, that substituted in (28) gives

$$\begin{aligned} \dot{x} &= \begin{cases} \Delta + 2R_-(y - c_-)x - Jrx; \ \forall y \leq V^\star \\ \Delta + 2R_+(y - c_+)x - Jrx; \ \forall y > V^\star, \end{cases} \\ \dot{y} &= \begin{cases} R_-(y - c_-)^2 + I_- - R_- x^2 + Jr(E - y) + \overline{\eta}; \ \forall y \leq V^\star \\ R_+(y - c_+)^2 + I_+ - R_+ x^2 + Jr(E - y) + \overline{\eta}; \ \forall y > V^\star, \end{cases} \end{aligned} \tag{29}$$

which is a reduction of a system of infinite all-to-all coupled neurons described by a step-wise quadratic equation.

Mean-field approximation of coupled neurons with biophysical nullclines

From equations (13) and (22), $y(t) \equiv V(t)$ represents the average membrane potential of the population, while $x(t)$ is an auxiliary variable, related to the firing rate as $r(t) = R_- x(t)/\pi$ (see previous section *Mean-field variables and firing rate*). Finally, starting from equation (29) we can replace the step-wise quadratic approximation with the original functional form (1) in the mean-field model, and reintegrate the dynamics of the other variables $\Delta[K^+]_{int}$, $[K]_g$. The mean-field approximation for a

population of HH neurons consists of a five-dimensional system:

$$
\begin{aligned}
\frac{dx}{dt} &= \begin{cases} \Delta + 2R_-(V-c_-)x - Jrx;\ \forall V \leq V^\star \\ \Delta + 2R_+(V-c_+)x - Jrx;\ \forall V > V^\star, \end{cases} \\
\frac{dV}{dt} &= \begin{cases} -\frac{1}{C_m}(I_{Cl}+I_{Na}+I_K+I_{pump}) - R_-x^2 + Jr(E_{syn}-V) + \overline{\eta};\ \forall V \leq V^\star \\ -\frac{1}{C_m}(I_{Cl}+I_{Na}+I_K+I_{pump}) - R_+x^2 + Jr(E_{syn}-V) + \overline{\eta};\ \forall V > V^\star, \end{cases} \\
\frac{dn}{dt} &= \frac{n_\infty(V)-n}{\tau_n}, \\
\frac{d\Delta[K^+]_{int}}{dt} &= -\frac{\gamma}{\omega_i}(I_K - 2I_{pump}), \\
\frac{d[K^+]_g}{dt} &= \varepsilon([K^+]_{bath} - [K^+]_{ext}\}).
\end{aligned}
\tag{30}
$$

Stimulation and coupling of neural mass models

In this work, the stimulation of the population is modeled by a common component $I_{input}(t)$ added to the membrane potential in Eq. 30 as:

$$
\frac{dV}{dt} = \frac{dV}{dt} + JI_{input}(E_{syn} - V). \tag{31}
$$

Accordingly, N populations described by Eq. 30 can be coupled together via their firing rate activity, so that the membrane potential equation at population P becomes:

$$
\frac{dV_P}{dt} = \frac{dV_P}{dt} + G\sum_Q W_{PQ} r_Q (E_{syn} - V_P), \tag{32}
$$

where W_{PQ} is the structural weight proportional to the white matter fiber tract density between populations P and Q, and G is the global coupling tuning the impact of the macroscopic network structure over the local dynamics.

The dynamics of single neuron and single mean-field population were simulated in *Python*. Spiking neural network simulations were performed using *Brain2* package. Connectome-based simulations were run using The Virtual Brain platform (Sanz-Leon et al., 2015). In Table S1, we detail all the parameters and the values of the initial conditions used in the reported results.

Results

Mean-field approximation and Spiking Neural Network simulation

In this work, we have derived a mean-field approximation of a locally homogeneous network of Hodgkin–Huxley type neurons (HH neuron) with heterogeneous quenched external input η (Eq. (30)). The accuracy of the mean-field approximation is validated by comparing it to the simulation of a large network of coupled HH neurons. The simulation of Hodgkin–Huxley type single neuron dynamics (Eq. (1)) driven by an ion-exchange mechanism, has revealed that the parameter $[K^+]_{bath}$ has the most significant impact on the dynamics (Fig. 2.a). Thus, for different $[K^+]_{bath}$ we simulated a network of $N = 3000$ coupled neurons described by Eq. (1), coupled as in Eq.(9) with synaptic strength $J = 1$ and receiving a heterogeneous quenched external input distributed with average value $\bar{\eta} = 0$ and distribution width $\Delta = 1$. Using the mean-field equations Eq.(30), we show that for different $[K^+]_{bath}$ values it is possible to define an effective parameter $[K^+]^{eff}_{bath}$ such that the mean-field model membrane potential V_{MF} matches qualitatively the average membrane potential V_{pop} of the neuronal population (Fig. 3.a). In Fig. 3.b we report the $[K^+]^{eff}_{bath}$ for two values of synaptic strength $J = 0.1$ and $J = 1$. This result shows that the mean-field model can be used to simulate several regimes of activity and emulate the average dynamics of a large neuronal population in strongly synchronized regimes. Notice that in such strongly synchronized regimes the population average displays dynamics qualitatively similar to the single neuron simulation (Fig. 2.a). However, due to the network effects in the population, there is a frequency shift with respect to the single neuron dynamics (for example the bursts in the $[K^+]_{bath} = 7.5$ regime are ~ 3 times faster in the population Fig. 3.a than in the single neuron Fig. 2.a). The definition of an effective $[K^+]^{eff}_{bath}$ adjusts this frequency shift. This fact echoes the physics concept of renormalization group flow, whereby the same model used to describe a single neuron ($N = 1$) can be used to describe the system at different scales (e.g., $N = 3000$), provided that the model constants are appropriately re-scaled (running coupling constants). Importantly, our neural mass model is capable of displaying complex

activity regimes which are not typical of the single neuron dynamics, and therefore emergent from the network interactions (see section *Emergent network states and multistability*).

Stepwise quadratic approximation for the nullcline results in extra mean-field parameters

To be able to apply convenient mathematical (analytical) methods in this study, the velocity of the membrane potential of a single neuron described by Eq. (1) was approximated as a step-wise quadratic function because the nullcline geometry resembles a combination of two inverted parabolas (Fig. 2 c) for different values of $[K^+]_{bath}$. In Supplementary Fig. S1(a) we show that the nullcline geometry resembles a cubic function for different constant values of the $\left(n, \Delta[K^+]_{int}, [K^+]\right)$ variables, and, therefore, it can be reasonably approximated by two inverted parabolas. Notably, after the thermodynamic limit the model equations Eq. (30) display four extra parameters (c_-, R_-, c_+, R_+) corresponding to the coefficients of the parabolas used in the step-wise quadratic approximation (Fig. 2.d). These parameters were fixed as constants based on a first approximation of the nullcline geometry (Eq. (19)). Tuning their values reflects qualitative changes in the mean-field dynamics such as frequency shifts and state transitions, as revealed by power spectral density analysis (Fig. 3.c).

Emergent network states and multistability

As we have shown, for different regimes of $[K^+]_{bath}$ the mean-field model is able to mimic a large set of brain activities similar to those observed at the single neuron level, such as a spike train, tonic spiking, bursting, a seizure-like event, a status epilepticus-like event, and a depolarization block (such as in Fig. 3.a). However, numerical simulations of a neural network show that other regimes can emerge from the interactions of a large population of coupled neurons (e.g., Fig. 4.a-b). Notably, the biophysical neuron model above is capable to simulate qualitatively similar regimes of activity where, for example, the amplitude of the bursts is modulated in time. In Fig. 4.c we show one such regime, where the amplitude of the oscillations increases during the bursting phase. Here, the parameters $(C_m = 16, \tau_n = 8, \varepsilon = 0.0001, \gamma = 0.00025)$ were modified to match realistic timescales of the slow potassium variables. Notably, similar kinds of neuronal activities were observed in-vitro (Fig. 4.d).

Previous studies showed that changing the value of the concentration of the external potassium bath is responsible for qualitative changes in the dynamical behavior of a single neuronal system (Depannemaecker et al., 2021b), particularly discovering that multistability occurs in a specific $[K^+]_{bath}$ range. Here, we discovered in-vitro evidence for two quasi-stable levels of external potassium variables (Fig. 5.a). A first state, lasting several minutes, can be identified as starting after the first arrow, which corresponds to the time when the concentration of magnesium was experimentally decreased. The second state, starting at the double-arrow, was spontaneously initiated and also lasted several minutes before transitioning to an oscillatory state (dashed box). Remarkably, in the mean-field model we were able to reproduce this result, whereby the bifurcation analysis performed by evaluating the average mean-field membrane potential for increasing $[K^+]_{bath}$ values and for two different initial conditions revealed two stable states, also in the healthy (i.e., without pathological bursting) regime e.g., for $[K^+]_{bath} = 5$ (Fig. 5.b).

Next, we again changed the parameters to show that the model is capable of showing complex burst modulation e.g., in the form of isolated bursts in the up-state (Fig. 5.c), qualitatively similar to those observed in-vitro (Fig. 5.a). In this configuration, we fixed $[K^+]_{bath} = 5$ in a healthy regime with the membrane potential remaining at its resting potential and stimulated the model with a progressively stronger (constant) input current. We observed that–even if in the healthy network configuration–certain amplitudes of external stimulus current could generate transient neuronal bursts and bistable behavior. The potential of the model in being affected by external input makes it suitable to be used as a neural mass for connectome-based simulations.

Coupled Neural Masses

Finally, we show that the presented mean-field model can be used to perform large-scale network simulations of brain activity e.g., to be used in the context of brain stimulation or epilepsy. To do so, we coupled six neural masses via long-range structural connections with random weights (Fig. 6.a). Each population (network node) is described by the mean-field model derived in this article (Eq. (30)). Nodes A, B, C, E, F are tuned to a healthy regime with $[K^+]_{bath} = 5.5$ which do not show pathological bursts when decoupled from other external inputs. Node D is tuned to a pathological regime $[K^+]_{bath} = 15.5$. We run a simulation of the system by setting the global coupling parameter to $G = 0$ (Fig. 6.b) and $G = 100$ (Fig. 6.c). In the first case, the system is effectively decoupled and, as expected, the only node displaying pathological activity is node D. However, in the second case, when G is increased, the system is coupled and the pathological fluctuations of node D differentially affect the activity of all other nodes at the whole-network level.

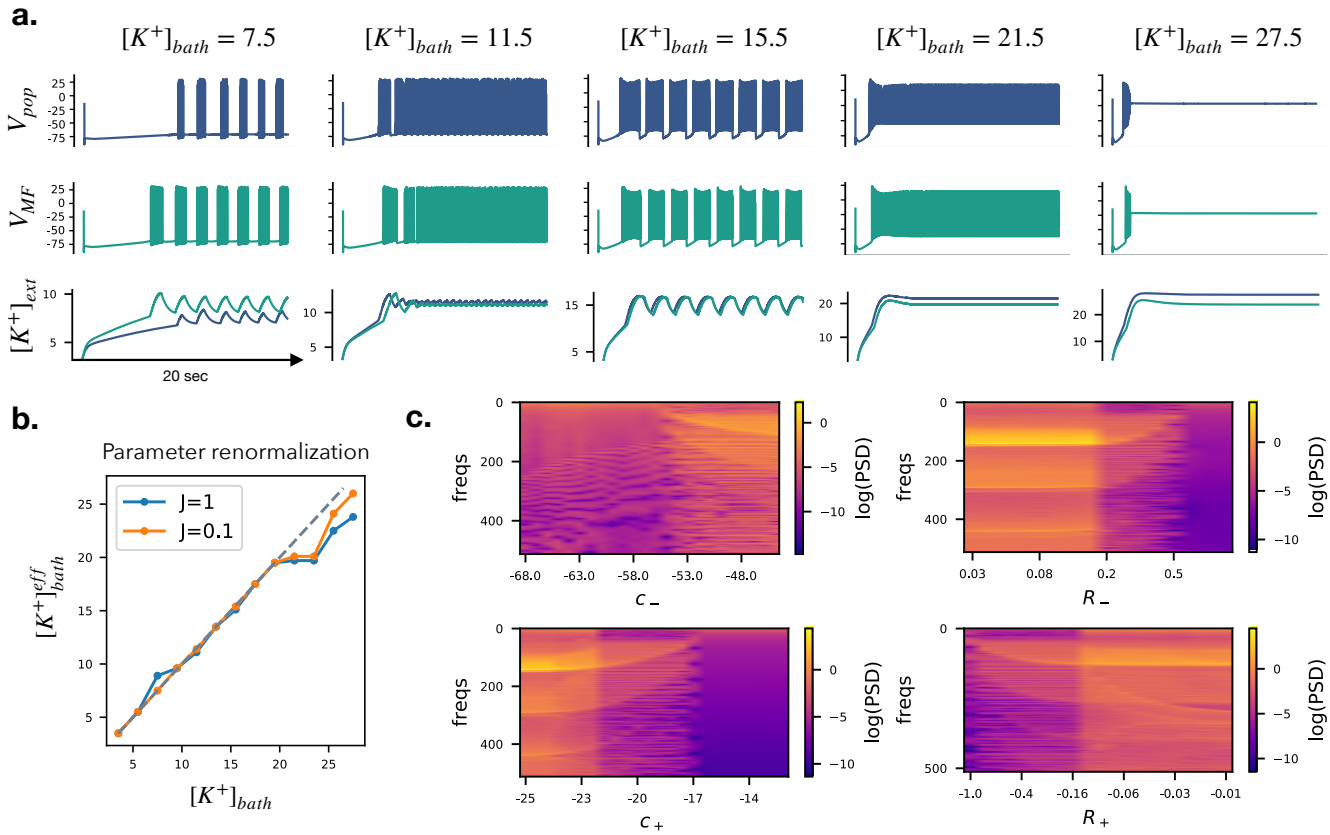

Figure 3. Meanfield model versus Neuronal network in strongly synchronized regimes: (a) For several $[K^+]_{bath}$ values we simulated the activity of a population of $N = 3000$ all-to-all coupled HH neurons in strongly synchronized regimes (parameters in TableS1). We compare the mean membrane potential V_{pop} and external potassium $[K^+]_{ext}$ of such population (in blue) with the results obtained using the mean-field model equations (in green). Notice that in order to properly match the slow timescale of the population, we defined an effective value of the potassium concentration in the bath $[K^+]^{eff}_{bath}$, represented in panel (b). (c) By changing the values of the parabola coefficients (c_-, R_-, c_+, R_+), which describe the nullcline geometry of the model, the results of the mean-field simulation change qualitatively. We show this parameters' effect by plotting the power spectral density for several values of these parameters (here we used $[K^+]_{bath} = 15.5$). We can observe that for all the parameters, frequency shifts and sudden state transitions occur.

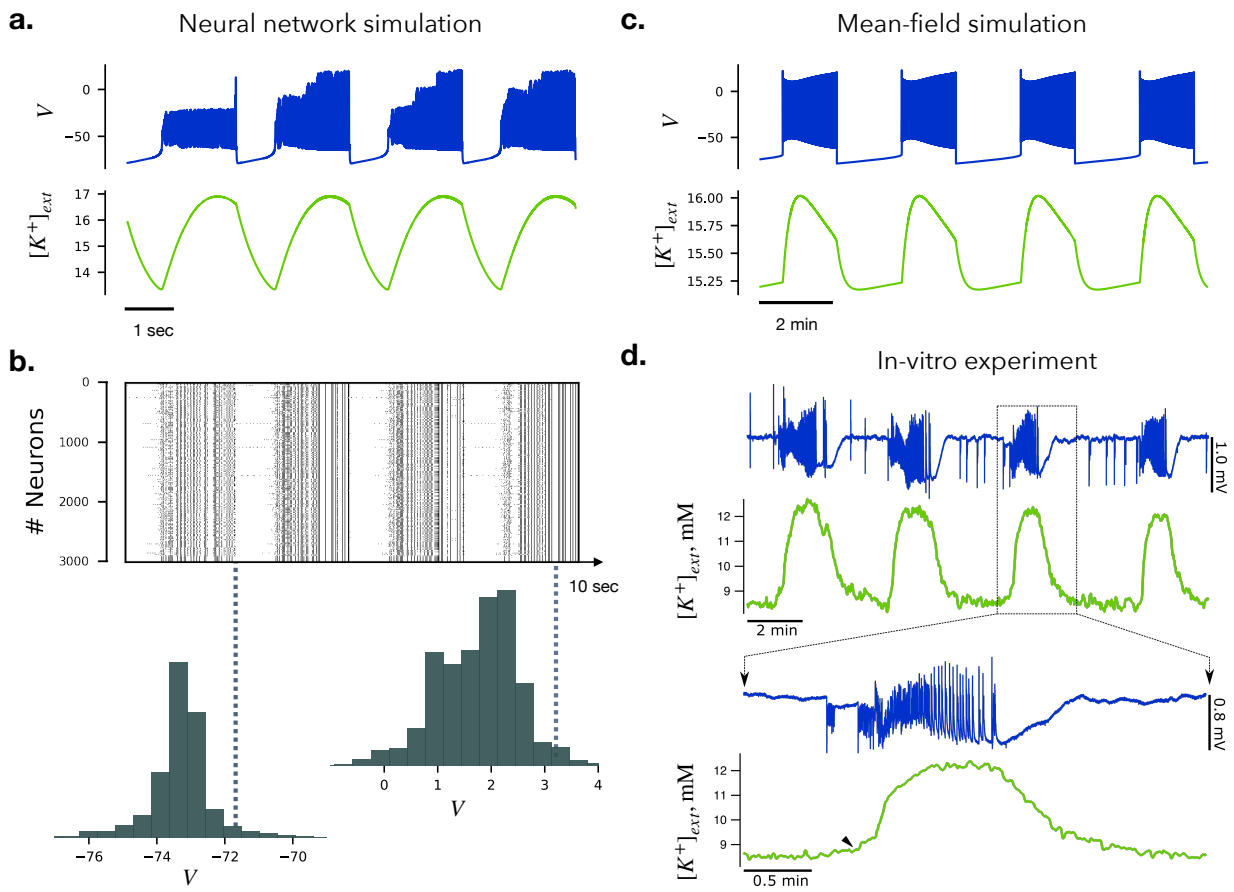

Figure 4. Comparison of numerical results and in-vitro experiments: (a) Mean membrane potential and external potassium concentration of a population of connected HH neurons. (b) Raster plot showing the membrane potential of neurons fluctuating above the threshold. At the bottom, we plot the membrane distribution for the population, as observed at two instants with low (left histogram) and high (right histogram) activity. (c) Mean field variables as simulated using the neural mass model. (d) Experimental co-recording of extracellular local field potential (blue traces) and extracellular K^+ concentration (green trace). The neuron model qualitatively reproduces the experimentally observed oscillations showing a modulation of the amplitude of the fast oscillations during a slow oscillation cycle. The matching of experimental timescales is possible by appropriate re-tuning of the neuron parameters C_m, τ_n, ε and γ (parameters in TableS1).

Limitations of the model

The approximation of the membrane potential dynamics as a step-wise quadratic function and the assumption of Lorentzian distributed membrane potential in the population allowed us to apply the Ott-Antonsen Ansatz and to develop the mean-field approximation of a heterogeneous network of biophysical neurons driven by ion-exchange dynamics coupled all-to-all via conductance-based coupling. With these approximations, the mean-field equations do not show a one-to-one correspondence with the neural network simulations, except in strongly synchronous regimes (Fig. 3.a). In fact, it is not guaranteed that such a population of HH neurons allows for a closed formulation of the thermodynamic limit. For example, the distribution of the membrane potentials resembles a Lorentzian only in some cases (e.g., Fig. 4.b, bottom left), while it can deviate from it in other moments (e.g., Fig. 4.b, bottom right). The mean-field model can be improved, for example by better exploring the parameter space defined by the parabola coefficients c_-, c_+, R_-, R_+, which here were fixed according to heuristic arguments (see Eq. (19)). In principle, these coefficients could be made functions of the slow variables, which might unveil new dynamical regimes and extend the validity of the thermodynamic limit beyond strongly synchronous regimes. The definition of the firing rate in the thermodynamic limit was approximated assuming a firing threshold for membrane potential going to infinity as in (20) and (21), however more refined definitions accounting for a heterogeneous firing threshold can be considered (Gast et al., 2022). In this work, we showed that the model can be used to retrieve emergent network behaviors similar to those observed in neuronal network simulations and *in-vitro*. This correspondence is not quantitative because the size of the network is finite, and, in experimental observations (in vivo/in vitro networks), the connectivity profile is not all-to-all connected. Despite its simplicity, the model displays desired properties such as bistability in healthy and pathological regimes (Fig. 5) and sensitivity to external coupling (Fig. 6). This approach, taking into account the biophysical aspect, offers a first step in considering the role of the glia in neural tissue excitability. Following this direction, other ions, such as calcium should be taken into consideration.

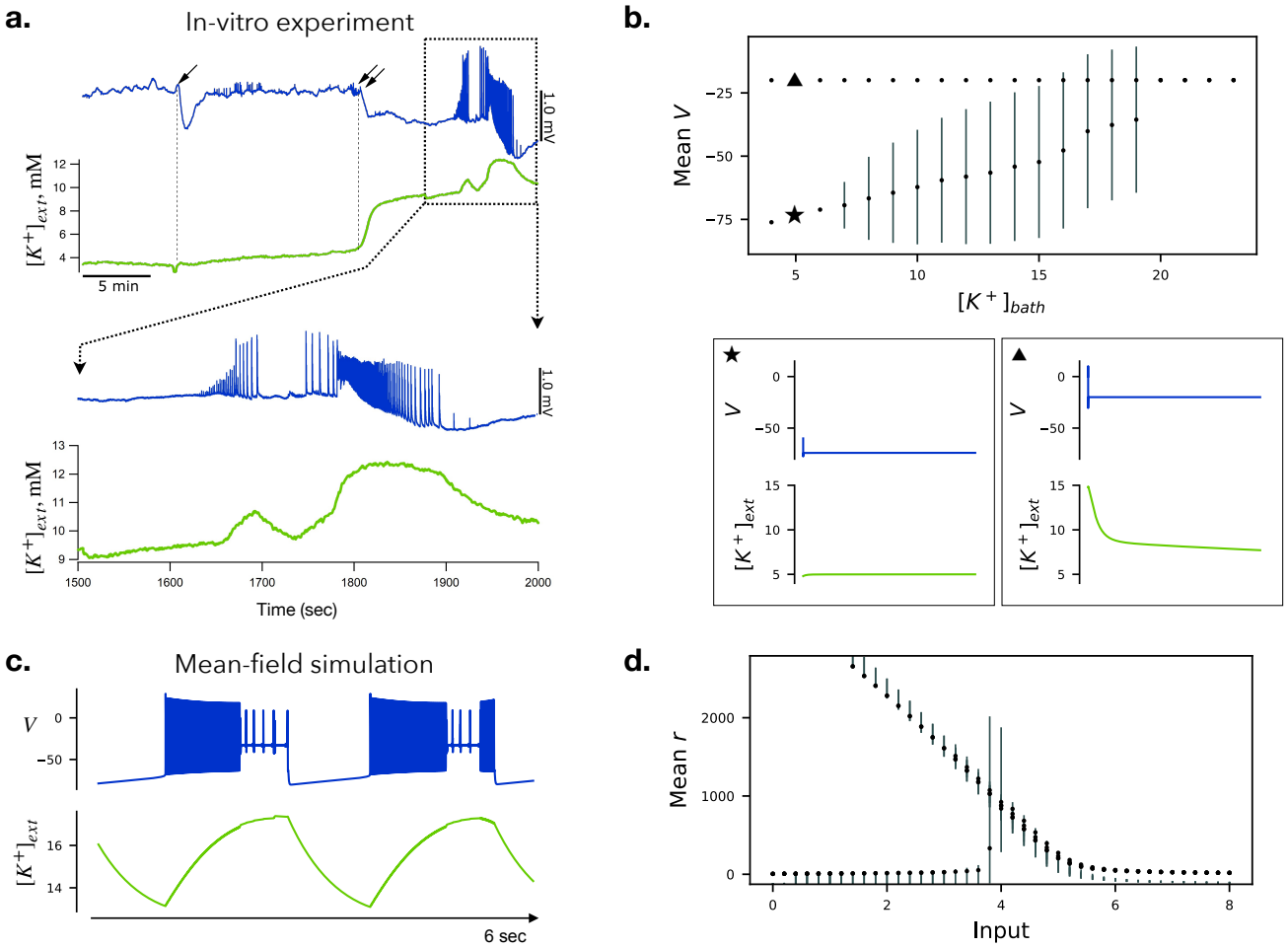

Figure 5. Bifurcation diagrams, emergent network states, and bistability: (a) In-vitro experiments show that the LFP (blue trace) is modulated by the extracellular concentration of potassium ions (green trace), fluctuating at a slow timescale. The external $[K^+]_{ext}$ concentration is relatively stable for several minutes (after the first black arrow that points on the onset of the low Mg^{2+} administration) before spontaneously transitioning towards a second similarly stable state (occurring at the double-arrow) with higher potassium concentration. From this state, after a few minutes, the ion concentration starts an oscillation that induces seizure-like events evidenced by the LFP recording. (b, top) A bifurcation diagram obtained by gradually varying the value of $[K^+]_{bath}$ shows that our model displays spontaneous multistable behavior across healthy and pathological regimes (parameters in TableS1). Each dot represents the mean membrane potential, simulated with a specific set of initial conditions. Vertical bars represent ± 1 standard deviation of the simulated membrane potential activity. (b, bottom) Example simulations for $[K^+]_{bath} = 5$ where the mean-field variables are initiated with two different initial conditions (black star and black triangle, respectively). Similarly to the *in-vitro* experiment in panel (a) the model can display burst-free 'healthy' behavior with two stable levels of external potassium concentration. (c) The mean-field model gives rise to an emergent behavior not present in the single-neuron model. In this example, the activity is characterized by a modulation of the bursting profile (parameters in TableS1). (d) Using the same parameters configuration as in panel (c), but starting from a healthy regime $[K^+]_{bath} = 5$–where the activity is confined into a fixed point–we show that for certain constant input current amplitudes the system enters into a bistable regime. Here each dot marks the average firing rate, and the vertical lines mark the maximum and minimum of the firing rate fluctuations in each condition.

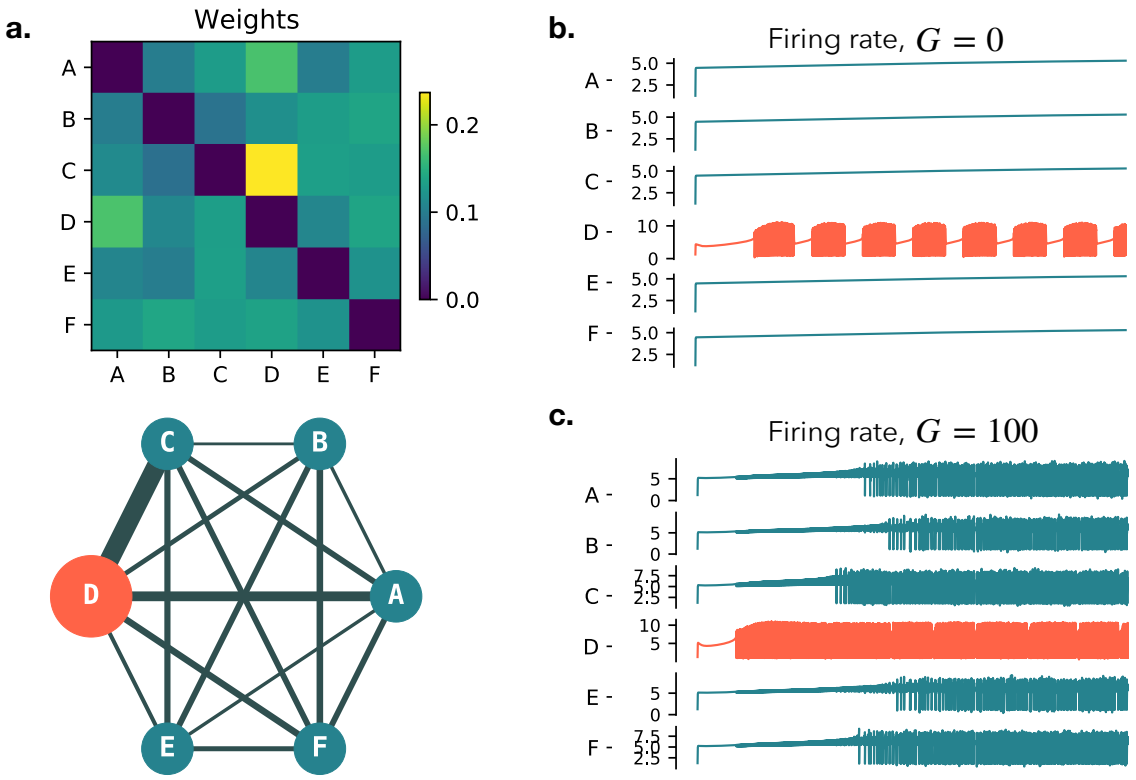

Figure 6. Network simulation of structurally connected neural mass models and propagation of pathological bursts: (a) Structural connectivity for six all-to-all connected nodes A, B, C, D, E, F with random weight allocation. Each node is described by a neural mass model derived as the mean-field approximation of a large population of HH neurons. (b) When decoupled (Global Coupling $G = 0$), all the nodes operate in a 'healthy' regime with the potassium concentration in their bath set to low values $[K^+]_{bath} = 5.5$, except for node D which is tuned into a pathological regime $[K^+]_{bath} = 15.5$ characterized by the spontaneous presence of bursts. (c) When the global coupling is sufficiently increased, the pathological value of $[K^+]_{bath}$ in node D generates bursts that diffuse through the connectome mimicking the spreading of a seizure.

Discussion

The general quest of modern neuroscience is understanding and explaining the mechanisms of different brain activities like perception, memory, and decision-making; but also more generally how the brain functions for healthy individuals during rest, and how it deviates from its healthy state in case of different diseases and disorders. Interestingly, most of these brain activities are accessed through measurements of brain dynamics that exhibit the collective electrical activities of a huge population of neurons demonstrating some interrelated electrical behavior in different brain regions. Therefore, brain activities, in general, can not be explained in microscopic terms (that is as the mechanism of a single neuron), rather they emerge at the macroscopic level as a result of the interaction between a large population of neurons. Also, besides the recent progress (Markram et al., 2015), it is still not possible to compute the behavior of a few billion such neurons (which comprises a mammalian brain), and even if it was, it remains questionable what knowledge would we gain from such a complex system (Frégnac, 2017). Hence, the most realistic way to model brain activities is to group a number of neurons together and write the mathematical descriptions for a group of neurons or large population (Sanz-Leon et al., 2015), using formalism from statistical physics and mathematics. In this case, we measure some property of the whole population, such as the mean membrane potential, rather than the activity of an individual neuron. Some of these properties do not even exist for an individual component, for example, temperature or pressure in case of molecular ensembles, order parameter (Kuramoto, 1984) and mean ensemble frequency (Petkoski et al., 2013) for coupled oscillators, or more specifically the firing rate in case of neuronal population (Gerstner and Kistler, 2002). However, to the best of our knowledge to date, there is no theory that can explain the behavior of a large population of neurons (brain areas) from the perspective of the driving mechanism of the neuronal activities, that is the ion exchange and transportation dynamics at the cellular level. Different pathological trials and experiments have already revealed that changes in ion concentration in brain regions could result in different brain dysfunction but the pathway of these phenomena is still unclear.

In this study, we developed a biophysically inspired mean-field model for a network of all-to-all connected, locally homogeneous Hodgkin–Huxley type neurons which are characterized by ion-exchange mechanism across the cellular space. The intermediate approximation into the step-wise quadratic function allowed us to apply the analytical formalism to the complex Hodgkin–Huxley type equations. The further assumption that the membrane potentials of neurons in a large population are distributed according to a Lorentzian (Lorentzian ansatz) makes the mean-field approximation analytically tractable. From the simulation of the network behavior of such neurons, it is evident that the mean-field model captures the dynamic behavior of the network when the population is highly synchronized. Furthermore, the mean-field model is capable of qualitatively capturing emergent neuronal network states observed in numerical simulations, as well as *in-vitro* (e.g., Fig. 4). The derived mean-field model relates the slow-timescale biophysical mechanism of ion exchange and transportation in the brain to the fast-timescale electrical activities of large neuronal ensembles. In fact, as demonstrated via brain imaging of different modalities (Rasmussen et al., 2020), ionic regulation acts on a relatively slow time scale on the fast electrical activity of neurons.

Analyzing the model, we found the potassium concentration in the external bath (parameter $[K^+]_{bath}$) and the heterogeneity of individual neurons in the population to be two significant determinants of the dynamics. Together, they take care of the biophysical state of the neuronal population (brain region) in terms of ion concentration and structural diversity. For low ion concentrations in the external bath, the mean-field model demonstrates the existence of healthy brain dynamics. Increasing the excitability in terms of ion concentration leads to the appearance of spike trains, tonic spiking, bursting, seizure-like events, status epilepticus-like events, and depolarization block, similar to the epileptor model (Jirsa et al., 2014, El Houssaini et al., 2015b, El Houssaini et al., 2020).

For several values of the potassium concentration in the external bath, or given an external input current, we showed that our model can be tuned into a bistable regime characterized by the coexistence of high and low firing rate states, which is the hallmark of many mean-field representations of linear (Di Volo et al., 2019, Zerlaut et al., 2018) or quadratic integrate and fire neurons (Coombes and Byrne, 2019, Montbrió et al., 2015), and rate models (Wong and Wang, 2006). Bistability is a desired feature for mean-field models. For example, bistability might provide a mechanism for the dynamic occurrence of so-called up (high firing) and down (low firing) states, as observed both *in vitro* (Plenz and Kitai, 1998, Cossart et al., 2003) and *in vivo* under several conditions such as quiet waking, anesthesia, slow-wave sleep and during perceptual task across several species (Steriade et al., 1993, Luczak et al., 2007, Vyazovskiy et al., 2011, Engel et al., 2016, Jercog et al., 2017). In fact, when bistable neural masses are coupled through a connectome and driven by a fine-tuned stochastic input noise, the simulated activities in brain regions can spontaneously jump between high and low firing rate states, which provides a mechanism for dynamic Functional Connectivity (Rabuffo et al., 2021), as observed in large-scale brain recordings (Preti et al., 2017).

Thus, the derived mean-field model links the presence of high and low firing rate states as well as the spiking and bursting neuroelectric behaviors with the biophysical state of the neuronal ensemble (brain regions) in terms of the ion concentrations across the cellular space. The effect of constant stimulus current is also analyzed and it is observed that even within the healthy regime, several stimulations, which could either correspond to external stimuli or inputs from some other brain regions, could generate transient spiking and bursting activity (Fig. 5.d). This result is particularly interesting in the case of brain stimulation. For example, several kinds of brain stimulation protocols in epileptic patients have already been found to generate epileptic

seizures in pathological practice (Fisher and Velasco, 2014, Kahane and Depaulis, 2010). Our results demonstrate that these phenomena could be reproduced and tracked in a modeling approach. Therefore, we assume that the derived model could potentially be applied to improve predictive capacities in several types of brain disorders, particularly epilepsy.

Using conductance-based coupling between six neuronal masses we also demonstrated that a hyper-excited population of neurons can propagate bursting and spiking behavior to otherwise healthy populations. This could lead the path to understanding how brain signals propagate as a coordinated phenomenon depending on the distribution of biophysical quantities and structural as well as architectural heterogeneity on the complex network structure of the connectome. Until now, mean-field models used in large-scale network simulations, like the Virtual Brain (Sanz-Leon et al., 2015), did not take into consideration the extracellular space. Our mean-field model is a first step towards the integration of biophysical processes that may play a key role in controlling network behavior, as shown at the spiking network level (Depannemaecker et al., 2022).

In this work, we focused on $[K^+]$, given its known role in neuronal activity. Changes in K^+ occur when the brain alternates between arousal and sleep (Ding et al., 2016). Although a causal relationship is not clearly established, seizures and spreading depression, which is assumed to underlie certain forms of migraine (Tottene et al., 2009, Vinogradova, 2018), are associated with large (>6 mM) and very large (>12 mM) concentrations of K^+ (Tottene et al., 2009, Hertz and Chen, 2016). The invariant increase of K^+ concentration during seizure (Heinemann et al., 1986), provokes a saturation of potassium buffering by the astrocytes. In fact, the extracellular concentration of K^+ is tightly controlled by astrocytes (Breslin et al., 2018, Nwaobi et al., 2016, Hansson et al., 2000). Most large-scale simulations do not integrate astrocytes, which make up half of the brain cells (Hansson et al., 2000, Breslin et al., 2018). Their functions are altered in most, if not all, brain disorders, in particular, epilepsy (Bedner and Steinhäuser, 2013, Crunelli et al., 2015). Our approach indirectly accounts for the astrocytic control of extracellular K^+. Other ion species also vary during arousal/sleep and seizures, in particular, Ca^{2+} (Ding et al., 2016, Pocock and Kettenmann, 2007, Auld and Robitaille, 2003, Fernandez-Chacon et al., 2001). A decrease in Ca^{2+} will decrease neurotransmission and thus change cell-to-cell communication (Pocock and Kettenmann, 2007, Auld and Robitaille, 2003, Fernandez-Chacon et al., 2001). Future studies are needed to integrate Ca^{2+} in neural mass models (NMM).

By addressing the biophysical information at the neuronal level, the mean-field formalism allows keeping biophysical interpretability while bridging between micro to macro-scale mechanisms. The mean-field model derived in this work aggregates a large class of brain activities and repertoire of patterns into a single neural mass model, with direct correspondence to biologically relevant parameters. This approach could serve as a computational baseline to address core questions in epilepsy research. In particular, how to identify the multiscale mechanisms implicated in epileptogenicity and propagation of seizures. This would eventually lead to establishing pathologically measurable bio-markers for large-scale brain activities and consequently offering therapeutic targets for different brain dysfunctions.

References

Amunts K, Mohlberg H, Bludau S, Zilles K (2020) Julich-Brain: A 3D probabilistic atlas of the human brain's cytoarchitecture. *Science* 369:988–992.

Amzica F, Massimini M, Manfridi A (2002) Spatial buffering during slow and paroxysmal sleep oscillations in cortical networks of glial cells in vivo. *Journal of Neuroscience* 22:1042–1053.

Ashwin P, Coombes S, Nicks R (2016) Mathematical frameworks for oscillatory network dynamics in neuroscience. *The Journal of Mathematical Neuroscience* 6:1–92.

Auld DS, Robitaille R (2003) Glial cells and neurotransmission: an inclusive view of synaptic function. *Neuron* 40:389–400.

Baladron J, Fasoli D, Faugeras O, Touboul J (2012) Mean-field description and propagation of chaos in networks of hodgkin-huxley and fitzhugh-nagumo neurons. *The Journal of Mathematical Neuroscience* 2:1–50.

Bandyopadhyay A, Kar S (2018) Impact of network structure on synchronization of Hindmarsh–Rose neurons coupled in structured network. *Applied Mathematics and Computation* 333:194–212.

Bazhenov M, Timofeev I, Steriade M, Sejnowski TJ (2004) Potassium model for slow (2-3 hz) in vivo neocortical paroxysmal oscillations. *Journal of neurophysiology* 92:1116–1132.

Bedner P, Steinhäuser C (2013) Altered kir and gap junction channels in temporal lobe epilepsy. *Neurochemistry international* 63:682–687.

Breslin K, Wade JJ, Wong-Lin K, Harkin J, Flanagan B, Van Zalinge H, Hall S, Walker M, Verkhratsky A, McDaid L (2018) Potassium and sodium microdomains in thin astroglial processes: A computational model study. *PLoS computational biology* 14:e1006151.

Byrne A, Brookes MJ, Coombes S (2017) A mean field model for movement induced changes in the beta rhythm. *Journal of computational neuroscience* 43:143–158.

Carlu M, Chehab O, Porta LD, Depannemaecker D, Héricé C, Jedynak M, Ersöz EK, Muratore P, Souihel S, Capone C, Zerlaut Y, Destexhe A, di Volo M (2020) A mean-field approach to the dynamics of networks of complex neurons, from nonlinear integrate-and-fire to hodgkin–huxley models. *Journal of Neurophysiology* 123:1042–1051.

Coombes S, Byrne Á (2019) Next generation neural mass models In *Nonlinear dynamics in computational neuroscience*, pp. 1–16. Springer.

Cossart R, Aronov D, Yuste R (2003) Attractor dynamics of network up states in the neocortex. *Nature* 423:283–288.

Courtiol J, Guye M, Bartolomei F, Petkoski S, Jirsa VK (2020) Dynamical mechanisms of interictal resting-state functional connectivity in epilepsy. *Journal of Neuroscience* 40:5572–5588.

Cressman JR, Ullah G, Ziburkus J, Schiff SJ, Barreto E (2009) The influence of sodium and potassium dynamics on excitability, seizures, and the stability of persistent states: I. single neuron dynamics. *Journal of computational neuroscience* 26:159–170.

Crunelli V, Carmignoto G, Steinhäuser C (2015) Novel astrocyte targets: new avenues for the therapeutic treatment of epilepsy. *The Neuroscientist* 21:62–83.

David O, Friston KJ (2003) A neural mass model for meg/eeg:: coupling and neuronal dynamics. *NeuroImage* 20:1743–1755.

Deco G, Jirsa VK (2012) Ongoing cortical activity at rest: criticality, multistability, and ghost attractors. *Journal of Neuroscience* 32:3366–3375.

Deco G, Jirsa VK, McIntosh AR (2011) Emerging concepts for the dynamical organization of resting-state activity in the brain. *Nature Reviews Neuroscience* 12:43–56.

Deco G, Jirsa VK, Robinson PA, Breakspear M, Friston K (2008) The dynamic brain: from spiking neurons to neural masses and cortical fields. *PLoS computational biology* 4:e1000092.

Deco G, Kringelbach ML, Arnatkeviciute A, Oldham S, Sabaroedin K, Rogasch NC, Aquino KM, Fornito A (2021) Dynamical consequences of regional heterogeneity in the brain's transcriptional landscape. *Science Advances* 7.

Depannemaecker D, Carlu M, Bouté J, Destexhe A (2022) A model for the propagation of seizure activity in normal brain tissue. *eneuro* pp. ENEURO.0234–21.2022.

Depannemaecker D, Destexhe A, Jirsa V, Bernard C (2021a) Modeling seizures: from single neurons to networks. *Seizure* .

Depannemaecker D, Ivanov A, Lillo D, Spek L, Bernard C, Jirsa V (2021b) A unified physiological framework of transitions between seizures, sustained ictal activity, and depolarization block at the single neuron level. *BioRxiv* pp. 2020–10.

Devalle F, Montbrió E, Pazó D (2018) Dynamics of a large system of spiking neurons with synaptic delay. *Physical Review E* 98:042214.

Di Volo M, Romagnoni A, Capone C, Destexhe A (2019) Biologically realistic mean-field models of conductance-based networks of spiking neurons with adaptation. *Neural computation* 31:653–680.

Ding F, O'donnell J, Xu Q, Kang N, Goldman N, Nedergaard M (2016) Changes in the composition of brain interstitial ions control the sleep-wake cycle. *Science* 352:550–555.

El Houssaini K, Bernard C, Jirsa VK (2020) The epileptor model: a systematic mathematical analysis linked to the dynamics of seizures, refractory status epilepticus, and depolarization block. *Eneuro* 7.

El Houssaini K, Ivanov AI, Bernard C, Jirsa VK (2015a) Seizures, refractory status epilepticus, and depolarization block as endogenous brain activities. *Physical Review E* 91:010701.

El Houssaini K, Ivanov AI, Bernard C, Jirsa VK (2015b) Seizures, refractory status epilepticus, and depolarization block as endogenous brain activities. *Physical Review E - Statistical, Nonlinear, and Soft Matter Physics* 91:2–6.

Engel TA, Steinmetz NA, Gieselmann MA, Thiele A, Moore T, Boahen K (2016) Selective modulation of cortical state during spatial attention. *Science* 354:1140–1144.

Fernandez-Chacon R, Königstorfer A, Gerber SH, García J, Matos MF, Stevens CF, Brose N, Rizo J, Rosenmund C, Südhof TC (2001) Synaptotagmin i functions as a calcium regulator of release probability. *Nature* 410:41–49.

Fisher RS, Velasco AL (2014) Electrical brain stimulation for epilepsy. *Nature Reviews Neurology* 10:261–270.

Frégnac Y (2017) Big data and the industrialization of neuroscience: A safe roadmap for understanding the brain? *Science* 358:470–477.

Fröhlich F, Timofeev I, Sejnowski TJ, Bazhenov M (2008) Extracellular potassium dynamics and epileptogenesis In *Computational neuroscience in epilepsy*, pp. 419–439. Elsevier.

Gast R, Solla SA, Kennedy A (2022) Macroscopic dynamics of neural networks with heterogeneous spiking thresholds. *arXiv preprint arXiv:2209.03501* .

Gerstner W, Kistler WM (2002) *Spiking neuron models: Single neurons, populations, plasticity* Cambridge university press.

Hansson E, Muyderman H, Leonova J, Allansson L, Sinclair J, Blomstrand F, Thorlin T, Nilsson M, Rönnbäck L (2000) Astroglia and glutamate in physiology and pathology: aspects on glutamate transport, glutamate-induced cell swelling and gap-junction communication. *Neurochemistry international* 37:317–329.

Heinemann U, Arens J (1992) Production and calibration of ion-sensitive microelectrodes. *Practical electrophysiological methods* pp. 206–212.

Heinemann U, Konnerth A, Pumain R, Wadman W (1986) Extracellular calcium and potassium concentration changes in chronic epileptic brain tissue. *Advances in neurology* 44:641–661.

Hertz L, Chen Y (2016) Importance of astrocytes for potassium ion (k+) homeostasis in brain and glial effects of k+ and its transporters on learning. *Neuroscience & Biobehavioral Reviews* 71:484–505.

Hocepied G, Legros B, Van Bogaert P, Grenez F, Nonclercq A (2013) Early detection of epileptic seizures based on parameter identification of neural mass model. *Computers in biology and medicine* 43:1773–1782.

Hodgkin AL, Huxley AF (1952) A quantitative description of membrane current and its application to conduction and excitation in nerve. *The Journal of physiology* 117:500–544.

Izhikevich EM, Edelman GM (2008) Large-scale model of mammalian thalamocortical systems. *Proceedings of the national academy of sciences* 105:3593–3598.

Jercog D, Roxin A, Bartho P, Luczak A, Compte A, de la Rocha J (2017) UP-DOWN cortical dynamics reflect state transitions in a bistable network. *eLife* 6:e22425.

Jirsa VK, Proix T, Perdikis D, Woodman MM, Wang H, Gonzalez-Martinez J, Bernard C, Bénar C, Guye M, Chauvel P et al. (2017) The virtual epileptic patient: individualized whole-brain models of epilepsy spread. *Neuroimage* 145:377–388.

Jirsa VK, Stacey WC, Quilichini PP, Ivanov AI, Bernard C (2014) On the nature of seizure dynamics. *Brain* 137:2210–2230.

Kahane P, Depaulis A (2010) Deep brain stimulation in epilepsy: what is next? *Current opinion in neurology* 23:177–182.

Krishnan GP, González OC, Bazhenov M (2018) Origin of slow spontaneous resting-state neuronal fluctuations in brain networks. *Proceedings of the National Academy of Sciences* 115:6858–6863.

Kuramoto Y (1984) *Chemical Oscillations, Waves, and Turbulence*, Vol. 19 of *Springer Series in Synergetics* Springer Berlin Heidelberg.

Laing CR (2017) Phase oscillator network models of brain dynamics. *Computational models of brain and behavior* 505:517.

Luczak A, Barthó P, Marguet SL, Buzsáki G, Harris KD (2007) Sequential structure of neocortical spontaneous activity in vivo. *Proceedings of the National Academy of Sciences* 104:347–352.

Luke TB, Barreto E, So P (2013) Complete classification of the macroscopic behavior of a heterogeneous network of theta neurons. *Neural computation* 25:3207–3234.

Markram H, Muller E, Ramaswamy S, Reimann MW, Abdellah M, Sanchez CA, Ailamaki A, Alonso-Nanclares L, Antille N, Arsever S, Kahou GAA, Berger TK, Bilgili A, Buncic N, Chalimourda A, Chindemi G, Courcol JD, Delalondre F, Delattre V, Druckmann S, Dumusc R, Dynes J, Eilemann S, Gal E, Gevaert ME, Ghobril JP, Gidon A, Graham JW, Gupta A, Haenel V, Hay E, Heinis T, Hernando JB, Hines M, Kanari L, Keller D, Kenyon J, Khazen G, Kim Y, King JG, Kisvarday Z, Kumbhar P, Lasserre S, Le Bé JV, Magalhães BRC, Merchán-Pérez A, Meystre J, Morrice BR, Muller J, Muñoz-Céspedes A, Muralidhar S, Muthurasa K, Nachbaur D, Newton TH, Nolte M, Ovcharenko A, Palacios J, Pastor L, Perin R, Ranjan R, Riachi I, Rodríguez JR, Riquelme JL, Rössert C, Sfyrakis K, Shi Y, Shillcock JC, Silberberg G, Silva R, Tauheed F, Telefont M, Toledo-Rodriguez M, Tränkler T, Van Geit W, Díaz JV, Walker R, Wang Y, Zaninetta SM, Defelipe J, Hill SL, Segev I, Schürmann F (2015) Reconstruction and Simulation of Neocortical Microcircuitry. *Cell* 163:456–492.

Melozzi F, Bergmann E, Harris JA, Kahn I, Jirsa V, Bernard C (2019) Individual structural features constrain the mouse functional connectome. *Proceedings of the National Academy of Sciences of the United States of America* 116:26961–26969.

Mody I, Lambert J, Heinemann U (1987) Low extracellular magnesium induces epileptiform activity and spreading depression in rat hippocampal slices. *Journal of neurophysiology* 57:869–888.

Montbrió E, Pazó D (2020) Exact mean-field theory explains the dual role of electrical synapses in collective synchronization. *Physical Review Letters* 125:248101.

Montbrió E, Pazó D, Roxin A (2015) Macroscopic description for networks of spiking neurons. *Physical Review X* 5:021028.

Moran RJ, Kiebel SJ, Stephan KE, Reilly R, Daunizeau J, Friston KJ (2007) A neural mass model of spectral responses in electrophysiology. *NeuroImage* 37:706–720.

Nevado-Holgado AJ, Marten F, Richardson MP, Terry JR (2012) Characterising the dynamics of eeg waveforms as the path through parameter space of a neural mass model: application to epilepsy seizure evolution. *Neuroimage* 59:2374–2392.

Nwaobi SE, Cuddapah VA, Patterson KC, Randolph AC, Olsen ML (2016) The role of glial-specific kir4. 1 in normal and pathological states of the cns. *Acta neuropathologica* 132:1–21.

Orkand RK, Nicholls JG, Kuffler SW (1966) Effect of nerve impulses on the membrane potential of glial cells in the central nervous system of amphibia. *Journal of Neurophysiology* 29:788–806.

Park EH, Durand DM (2006) Role of potassium lateral diffusion in non-synaptic epilepsy: a computational study. *Journal of theoretical biology* 238:666–682.

Petkoski S, Iatsenko D, Basnarkov L, Stefanovska A (2013) Mean-field and mean-ensemble frequencies of a system of coupled oscillators. *Physical Review E - Statistical, Nonlinear, and Soft Matter Physics* 87:1–12.

Petkoski S, Jirsa VK (2019) Transmission time delays organize the brain network synchronization. *Philosophical Transactions of the Royal Society A: Mathematical, Physical and Engineering Sciences* 377:20180132.

Petkoski S, Stefanovska A (2012) Kuramoto model with time-varying parameters. *Physical Review E* 86:046212.

Plenz D, Kitai ST (1998) Up and down states in striatal medium spiny neurons simultaneously recorded with spontaneous activity in fast-spiking interneurons studied in cortex–striatum–substantia nigra organotypic cultures. *Journal of Neuroscience* 18:266–283.

Pocock JM, Kettenmann H (2007) Neurotransmitter receptors on microglia. *Trends in neurosciences* 30:527–535.

Preti MG, Bolton TA, Van De Ville D (2017) The dynamic functional connectome: State-of-the-art and perspectives. *Neuroimage* 160:41–54.

Proix T, Bartolomei F, Chauvel P, Bernard C, Jirsa VK (2014) Permittivity coupling across brain regions determines seizure recruitment in partial epilepsy. *Journal of Neuroscience* 34:15009–15021.

Proix T, Bartolomei F, Guye M, Jirsa VK (2017) Individual brain structure and modelling predict seizure propagation. *Brain* 140:641–654.

Rabuffo G, Fousek J, Bernard C, Jirsa V (2021) Neuronal cascades shape whole-brain functional dynamics at rest. *Eneuro* 8.

Ransom CB, Ransom BR, Sontheimer H (2000) Activity-dependent extracellular k+ accumulation in rat optic nerve: the role of glial and axonal na+ pumps. *The Journal of physiology* 522:427–442.

Rasmussen R, Jensen MH, Heltberg ML (2017) Chaotic dynamics mediate brain state transitions, driven by changes in extracellular ion concentrations. *Cell Systems* 5:591–603.

Rasmussen R, Nicholas E, Petersen NC, Dietz AG, Xu Q, Sun Q, Nedergaard M (2019) Cortex-wide changes in extracellular potassium ions parallel brain state transitions in awake behaving mice. *Cell reports* 28:1182–1194.

Rasmussen R, O'Donnell J, Ding F, Nedergaard M (2020) Interstitial ions: A key regulator of state-dependent neural activity? *Progress in neurobiology* 193:101802.

Roxin A, Brunel N, Hansel D (2005) Role of delays in shaping spatiotemporal dynamics of neuronal activity in large networks. *Physical review letters* 94:238103.

Sanz-Leon P, Knock SA, Spiegler A, Jirsa VK (2015) Mathematical framework for large-scale brain network modeling in the virtual brain. *Neuroimage* 111:385–430.

Shriki O, Hansel D, Sompolinsky H (2003) Rate models for conductance-based cortical neuronal networks. *Neural computation* 15:1809–1841.

Spiegler A, Knösche TR, Schwab K, Haueisen J, Atay FM (2011) Modeling brain resonance phenomena using a neural mass model. *PLoS computational biology* 7:e1002298.

Steriade M, Nunez A, Amzica F (1993) A novel slow (<1 hz) oscillation of neocortical neurons in vivo: depolarizing and hyperpolarizing components. *The Journal of Neuroscience* 13:3252–3265.

Tottene A, Conti R, Fabbro A, Vecchia D, Shapovalova M, Santello M, van den Maagdenberg AM, Ferrari MD, Pietrobon D (2009) Enhanced excitatory transmission at cortical synapses as the basis for facilitated spreading depression in cav2. 1 knockin migraine mice. *Neuron* 61:762–773.

Touboul J, Wendling F, Chauvel P, Faugeras O (2011) Neural mass activity, bifurcations, and epilepsy. *Neural computation* 23:3232–3286.

Ullah G, Cressman Jr JR, Barreto E, Schiff SJ (2009) The influence of sodium and potassium dynamics on excitability, seizures, and the stability of persistent states: Ii. network and glial dynamics. *Journal of computational neuroscience* 26:171–183.

Vinogradova LV (2018) Initiation of spreading depression by synaptic and network hyperactivity: Insights into trigger mechanisms of migraine aura. *Cephalalgia* 38:1177–1187.

Vyazovskiy VV, Olcese U, Hanlon EC, Nir Y, Cirelli C, Tononi G (2011) Local sleep in awake rats. *Nature* 472:443–447.

Wendling F, Benquet P, Bartolomei F, Jirsa V (2016) Computational models of epileptiform activity. *Journal of neuroscience methods* 260:233–251.

Wilson HR, Cowan JD (1972) Excitatory and inhibitory interactions in localized populations of model neurons. *Biophysical journal* 12:1–24.

Wong KF, Wang XJ (2006) A recurrent network mechanism of time integration in perceptual decisions. *Journal of Neuroscience* 26:1314–1328.

Zerlaut Y, Chemla S, Chavane F, Destexhe A (2018) Modeling mesoscopic cortical dynamics using a mean-field model of conductance-based networks of adaptive exponential integrate-and-fire neurons. *Journal of computational neuroscience* 44:45–61.

Author contributions

A.B., G.R., S.P., and V.K.J. designed research; A.B., G.R., C.C., K.G., D.D., S.P., and V.K.J. performed research; A.B., G.R., C.C., K.G., D.D. simulated the models and analyzed the results; G.R. designed the figures. A.I. performed the experiments. A.B., G.R., D.D., A.I., C.B., S.P., and V.K.J. wrote the paper. *A.B. and *G.R. contributed equally to this work as first authors. +S.P. and +V.K.J. contributed equally to this work as the last authors. The authors declare no competing financial interests. Correspondence should be addressed to Spase Petkoski at spase.petkoski@univ-amu.fr or Viktor K. Jirsa at viktor.jirsa@univ-amu.fr.

Acknowledgments

We thank Prof.Marja-Leena Linne for the useful comments and the rich discussions on this work.
This research was supported by the European Union's Horizon 2020 research and innovation program under grant agreement 945539 (SGA3) Human Brain Project and by grant agreement No. 826421 Virtual Brain Cloud. CB received support from the Agence Nationale de la recherche projects ANR-17-CE37-0001-01 and ANR-20-NEUC-0005-02.

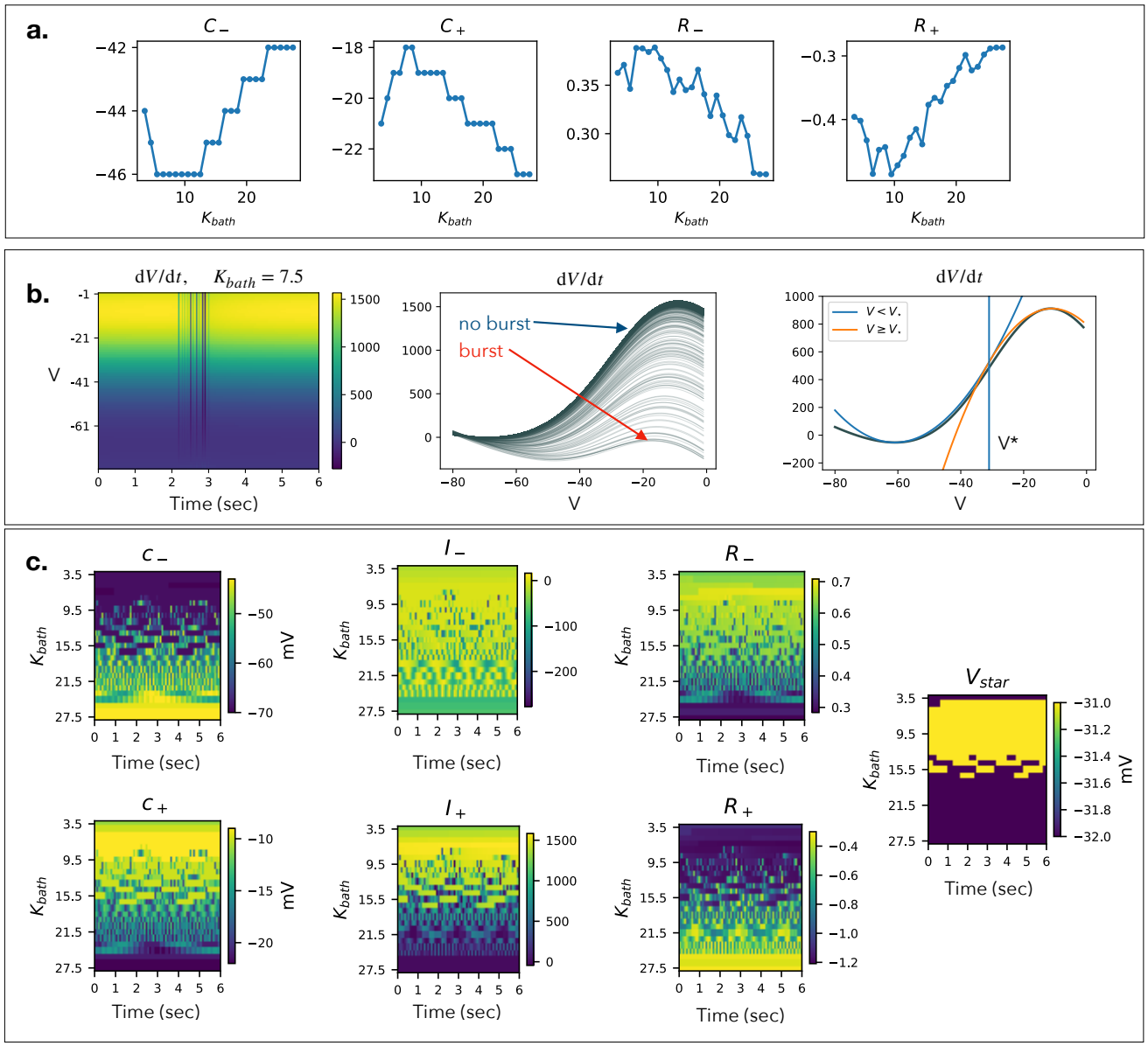

Figure S1. Quadratic approximation of nullcline geometry: (a) In Fig. 4.b we showed that the nullcline geometry of the single neuron can be approximated by two inverted parabolas. Panel (a) shows the coefficients of the parabolas (c_-, R_-) and (c_+, R_+) as functions of $[K^+]_{bath}$ corresponding to Fig. 4.a. (b) At each simulation time of the single neuron dynamics ($[K^+]_{bath} = 7.5$) we evaluated the variable $n, \Delta[K^+]_{int}$ and $[K^+]_g$ and fixed them as constants. Then we evaluated the membrane potential equation $\mathrm{d}V/\mathrm{d}t$ for different values V. At different times (and different $n, \Delta[K^+]_{int}$ and $[K^+]_g$ values) the equation resembles a cubic function. We can model these functions as step-wise quadratic functions, corresponding to two parabolas with vertices at coordinates (c_-, I_-) and (c_+, I_+) and curvature R_- and R_+, respectively. The two parabolas meet at an intersection point $V^\star$ where the membrane potential equation changes curvature. (c) For each time point and each $[K^+]_{bath}$, we estimated the parabola coefficients.

	Fig.2.a	**Fig.3.a**	**Fig.4.a-b**	**Fig.4.c**	**Fig.5.b-d**	**Fig.5.c**	**Fig.6.b-c**
Δ	-	1	1	1	1	1	1
$\mathbf{J}$	-	1	1	0.01	0.01	2	0.08
η	-	0	0	0	1	0	0
K_{bath}	-	-	15.5	15.5	-	15.5	-
c_-	-	-44.24	-	-44.24	-40	-44.24	-44.24
c_+	-	-20.40	-	-20.40	-20	-20.40	-20.40
R_-	-	0.34	-	0.001	0.01	0.50	0.02
R_+	-	-0.38	-	-0.01	-0.40	-0.50	-0.1
C_m	1	1	10	16	1	1	1
τ_n	4	4	2.4	8	4	4	4
γ	0.04	0.04	0.04	0.00025	0.004	0.04	0.04
ε	0.001	0.001	0.001	0.0001	0.001	0.001	0.001
$x(t=0)$	-	-	0.17	36.81	-	0.10	0.10
$V(t=0)$	-5	-15	-81.78	-70.82	-	-15	-15
$n(t=0)$	0.40	0.45	0.03	0.05	-	0.45	0.45
$\Delta K_i(t=0)$	-0.10	-3.50	-4.92	-0.23	-	-5	-5
$K_g(t=0)$	3	-12	-14.88	7.93	-	-16	-16
$\mathbf{N}$	1	3000	3000	-	-	-	-

Table S1. List of parameters' values used for each simulation in the manuscript. If not present, the parameter is not applicable for that case, or different values have been used, as specified in the corresponding caption.